RSC Advances

PAPER

View Article Online
View Journal | View Issue

Cite this: *RSC Adv.*, 2025, **15**, 33494

A supramolecular semiconducting nickel(II)-metallohydrogel with dual antimicrobial and micro-electronic device applications

Subhendu Dhibar,†*[a] Aiswarya Mohan,†[b] Rajlakshmi Laha,†[c] Sangita Some,[a] Priya Kaith,[d] Aditi Trivedi,[e] Subham Bhattacharjee,[f] Lebea N. Nthunya,[g] Timothy O. Ajiboye,[h] Ashok Bera,[d] Sumit Kumar Panja,[i] Asit Kumar Das,[j] Somasri Dam,*[c] Padmanabhan Predeep*[k] and Bidyut Saha*[a]

A multifunctional Ni(II)-based metallohydrogel (NiC-GT) was developed by reacting nickel(II) chloride with guanylthiourea in water under ambient conditions. The resulting hydrogel exhibited excellent mechanical stability, as validated by comprehensive rheological and thixotropic analyses. Field emission scanning electron microscopy (FESEM) revealed a well-organized hierarchical microstructure, while energy-dispersive X-ray (EDX) mapping confirmed the uniform distribution of key elements such as C, N, O, S, Cl, and Ni within the gel matrix. Fourier-transform infrared (FT-IR) spectroscopy provided insights into the non-covalent interactions driving gelation, and powder X-ray diffraction (PXRD) analysis demonstrated the semi-crystalline characteristics of the material. Optical absorption studies indicated the semiconducting behaviour of the hydrogel, with enhanced electron mobility surpassing that of comparable soft materials. Notably, the hydrogel displayed broad-spectrum antibacterial efficacy against both Gram-positive (*Bacillus subtilis*, *Staphylococcus aureus*) and Gram-negative (*Escherichia coli*, *Pseudomonas aeruginosa*) bacterial strains, suggesting its effectiveness in biomedical contexts. The integration of mechanical robustness, semiconducting functionality, and antimicrobial activity positions this Ni(II)-metallohydrogel as a promising candidate for emerging applications in flexible electronic devices, biosensors, and therapeutic systems. This work highlights the synergistic potential of transition metal-coordinated supramolecular systems for advancing smart soft material platforms.

Received 28th June 2025
Accepted 3rd September 2025

DOI: 10.1039/d5ra04603c

rsc.li/rsc-advances

1. Introduction

Gels are a distinctive class of soft matter, characterized by their ability to entrap substantial amounts of liquid within a three-dimensional structural network.[1] This unique capability is attributed to gelator molecules that self-assemble into stable matrices through various types of cross-linking interactions.[2] The formation of gels is often complex and unpredictable, sometimes occurring through unanticipated or serendipitous processes, which continues to intrigue researchers in materials science.[3] A widely used method for assessing gelation is the "tube inversion test".[3] In this simple yet effective approach, if the material does not flow when the container is inverted, it signifies that a gel has formed. What sets gels apart is their hybrid nature-they exhibit the rigidity of solids while maintaining the fluidity of liquids. This duality imparts them with exceptional physicochemical properties. Due to these attributes, gels have garnered significant interest for a broad range of applications, including biomedical devices, drug delivery systems, food technology, cosmetics, and the creation of next-generation functional materials.[4] Their versatility and

[a]*Colloid Chemistry Laboratory, Department of Chemistry, The University of Burdwan, Golapbag, Burdwan-713104, West Bengal, India. E-mail: sdhibar@scholar.buruniv.ac.in; bsaha@chem.buruniv.ac.in; Tel: +91 9476341691; +91 7001575909*

[b]*Laboratory for Molecular Photonics and Electronics (LAMP), Department of Physics, National Institute of Technology Calicut, Calicut-673603, Kerala, India*

[c]*Department of Microbiology, The University of Burdwan, Burdwan-713104, West Bengal, India. E-mail: sdam@microbio.buruniv.ac.in*

[d]*Department of Physics, Indian Institute of Technology Jammu, J&K-181221, India*

[e]*National Institute of Science Education and Research (NISER), Bhubaneswar, Odisha 752050, India*

[f]*Department of Chemistry, Kazi Nazrul University, Asansol-713303, West Bengal, India*

[g]*Institute for Nanotechnology and Water Sustainability, University of South Africa, Florida Science Campus, 1709 Roodepoort, South Africa*

[h]*Faculty of Natural and Agricultural Sciences, North-West University, Mmabatho-2735, South Africa*

[i]*Tarsadia Institute of Chemical Science, Uka Tarsadia University, Surat-394350, Gujrat, India*

[j]*Department of Chemistry, Murshidabad University, Berhampore-742101, West Bengal, India*

[k]*School of Nanoscience and Nanotechnology, Mahathma Gandhi University, Kottayam-686560, Kerala, India. E-mail: predeep@mgu.ac.in*

† S. D, A. M. and R. L should be treated as joint first authors.

adaptive nature continue to inspire innovation in multiple scientific and industrial fields.

Gels are broadly categorized into two primary types based on their network formation mechanisms: chemically cross-linked gels and supramolecular or physical gels. Chemically cross-linked gels are constructed through strong covalent bonds, resulting in rigid, often non-reversible structures.[5] In contrast, supramolecular gels arise from the self-organization of low-molecular-weight gelator molecules, usually less than 3000 Daltons.[6,7] These gelators assemble into networks through reversible, noncovalent interactions, including hydrogen bonding, π–π stacking, van der Waals forces, and various electrostatic forces such as cation–π, anion–π, dipole–dipole, and ion–dipole interactions.[8–13] These noncovalent forces impart dynamic and tunable properties to supramolecular gels.

The structural design of the gelator is fundamental to the success of the gelation process. A broad spectrum of low molecular weight gelators (LMWGs) has been explored for forming supramolecular gels, including urea-based compounds,[14] dicarboxylic acids,[15] functionalized amino acids,[16] fatty acids,[5] dendritic structures,[17] sorbitol,[17] and carbohydrates.[17] In addition to the gelator's design, the solvent plays a critical role by serving not only as a dispersion medium but also by directly influencing the self-assembly behavior of the gelator molecules. The physicochemical properties of the solvent, such as polarity, viscosity, hydrogen bonding potential, and coordination ability, significantly affect the gel's structural features, including fiber thickness, network morphology, and mechanical stability. Consequently, solvent selection becomes vital in optimizing gel formation. Common solvents utilized in supramolecular gel studies include water,[18–23] various alcohols,[24] dimethylformamide (DMF),[25–32] dimethyl sulfoxide (DMSO),[33] acetonitrile,[34] and acetone,[35] all of which have been found effective in facilitating the formation of stable and structured gel systems.

Metallohydrogels are an emerging and innovative subclass of supramolecular gels, distinguished by the incorporation of metal ions or metal-based complexes that coordinate with organic molecules to form organized, three-dimensional networks.[36] These gels are commonly formed through the interaction of low molecular weight gelators (LMWGs) with various transition metal ions, resulting in hybrid materials with enhanced physical and functional properties. Transition metals such as copper(II),[37] nickel(II),[38,39] cobalt(II),[40] zinc(II),[41] iron(II/III),[42] cadmium(II),[43] mercury(II),[43–46] and manganese(II) have been widely utilized in designing these metallogels. The coordination of metal centers not only strengthens the gel's internal framework but also imparts a range of additional functionalities. These include redox responsiveness,[47] catalytic efficiency,[18,19] magnetic characteristics,[48] treatment of dental caries,[49] remodeling growth plate of children,[50] cartilage repair,[51] and the capacity to act as scaffolds for nanoparticle generation.[52] Such multifunctional capabilities make metallohydrogels promising candidates for applications in areas like catalysis, environmental remediation, sensing, and biomedical engineering. Their rapid development underscores their importance in advanced materials science.

The choice of ligand plays a pivotal role in the formation of metallohydrogels. Ligands with multiple coordinating groups-such as amino, hydroxyl, or carboxylate functionalities-are particularly suited for gel formation.[53] In a notable study from 2014, Prof. Tarasankar Pal and his team successfully synthesized a copper-based metallogel using thiourea in water and demonstrated its utility in the visual detection of picric acid.[54] Building upon this concept, guanylthiourea, recognized for its strong coordination ability, serves as an effective ligand for metallohydrogel formation, as demonstrated in our synthesis of a novel Ni(II)-based metallohydrogel under mild aqueous conditions. The hydrogel forms rapidly, producing a stable orange-coloured material. The gel matrix is primarily stabilized by coordination bonds between Ni(II)-ions and guanylthiourea ligands, further reinforced by intermolecular hydrogen bonding among the gelator molecules. The resulting hydrogel exhibits high structural integrity, reproducibility, and a homogenous network, making it a promising candidate for next-generation functional materials. Nickel(II) was specifically chosen over other transition metals due to its exceptional electronic configuration and strong coordination tendency with nitrogen- and sulfur-containing ligands, which facilitate the formation of stable, highly ordered networks. Moreover, Ni(II)-based systems possess inherent semiconducting properties that enable efficient charge transport, while simultaneously exhibiting broad-spectrum antibacterial activity through interaction with microbial enzymes and cell membranes. This unique combination of semiconducting and antimicrobial functionality renders Ni(II)-derived metallohydrogels particularly attractive for next-generation electronic and biomedical applications.

In particular, metallohydrogels have shown significant promise in Schottky diode applications due to their adaptable electronic characteristics, environmental stability, and ease of integration with existing electronic fabrication methods. By carefully tuning the metal–ligand interactions, electronic performance can be enhanced. Their multifunctional nature supports the development of diverse electronic and optoelectronic devices. In recent advancements, Dhibar and colleagues introduced a facile and efficient method to produce metallogels without relying on extreme synthesis conditions, maintaining both performance and stability.[18–23,25–32] The Ni(II)-based metallohydrogel developed through this method demonstrates impressive electrical conductivity, favourable optoelectronic responses, and strong antibacterial activity. Detailed investigations into its mechanical properties and nanostructure further emphasize its potential in semiconducting and biomedical device applications.

2. Experimental

2.1. Materials

Nickel(II) chloride hexahydrate (Sigma-Aldrich, USA, 99.99% trace metals basis), guanylthiourea (Sigma-Aldrich, USA, 99%), were utilized as received. Throughout the study, triple-distilled water was used for all experimental procedures. Tryptone, D-(+)-Glucose anhydrous, and Yeast Extract Powder were obtained from Himedia.

2.2. Apparatus and measurements

2.2.1. Rheological analysis. Rheological experiments were performed using a cone-plate geometry with a fixed gap of 0.5 mm. The hydrogel samples were gently loaded onto the rheometer plate to preserve their structure. A strain amplitude sweep was first conducted at a constant frequency of 1 Hz, with the strain varying from 0.001% to 100% at 25 °C to determine the linear viscoelastic region (LVR). Following this, frequency sweep tests were carried out within the established LVR at a constant strain of 0.01% to accurately characterize the gel's intrinsic viscoelastic properties without disrupting its network structure.

2.2.2. Field emission scanning electron microscopic (FESEM) study. The metallohydrogel was carefully drop-cast onto a pre-cleaned glass substrate and allowed to dry naturally at room temperature overnight. Once dried, the samples were coated with a thin layer of gold using a vapor deposition technique. Surface morphology was examined using a Carl Zeiss SUPRA 55VP scanning electron microscope operated at an accelerating voltage between 10 and 15 kV. Elemental composition analysis was conducted using energy-dispersive X-ray spectroscopy (EDX) on a ZEISS EVO 18 system.

2.2.3. FT-IR study. Infrared spectra in the range of 4000–500 cm^{-1} were obtained using a JASCO FTIR 4700 spectrophotometer, with the samples prepared as KBr pellets.

2.2.4. PXRD study. The structural characteristics of the metallohydrogel were examined using a PANalytical X'Pert powder X-ray diffractometer equipped with Cu Kα1 radiation.

2.2.5. IV characteristics. The IV characteristics of the device were recorded using a Keithley 2400 source meter connected to a computer.

2.3. Synthesis of Ni(II)-guanylthiourea based metallohydrogel (NiC-GT)

At room temperature, an aqueous solution of bright green nickel(II) chloride hexahydrate (0.237 g, 1 mmol, ~500 μL) was quickly mixed with a transparent aqueous solution (~500 μL) of guanylthiourea (0.118 g, 1 mmol). This immediate combination resulted in the rapid formation of an orange-coloured nickel(II)-based metallohydrogel, designated as NiC-GT. A schematic representation of the proposed NiC-GT hydrogel network, along with an inverted vial photograph demonstrating its stable gel phase, is presented in Fig. 1. The initial confirmation of gelation and structural robustness was achieved using the inverted vial technique (Fig. 1), which was subsequently validated through comprehensive rheological studies described in later sections.

To evaluate the minimum concentration required for gel formation, the critical gelation concentration (MGC) of the NiC-GT system was determined by varying the concentrations of $NiCl_2 \cdot 6H_2O$ and guanylthiourea between 20 and 355 mg mL^{-1}, while maintaining a fixed 1 : 1 mass ratio. A uniform and stable deep orange gel consistently formed at 355 mg mL^{-1} of each component in water. The thermal stability of the resulting metallohydrogel was investigated using a digital melting point apparatus. The gel remained structurally intact up to approximately 80 ± 2 °C, beyond which it transitioned to the sol state, demonstrating notable thermal robustness.

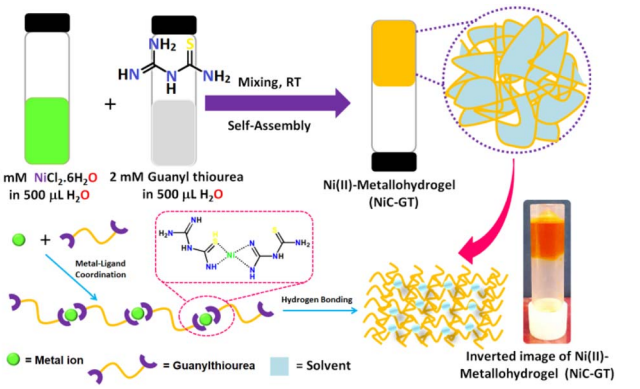

Fig. 1 The gelation process follows the outlined synthetic pathway, ultimately leading to the formation of the Ni(II)-based metallohydrogel (NiC-GT). A photographic image, accompanied by a schematic diagram, visually depicts the resulting NiC-GT metallohydrogel.

2.4. Antimicrobial activity of NiC-GT

Antimicrobial activity of NiC-GT metallohydrogel was checked against different bacterial strains. Gram-negative bacterial strains *Escherichia coli, Pseudomonas aeruginosa* and Gram-positive strains *Bacillus subtilis* and *Staphylococcus aureus* have been taken for antibacterial screening. Streptomycin, a conventional broad spectrum antibiotic, has been used as positive control.

In this experiment 100 μL of bacterial inoculum from log phase culture was evenly distributed on the solid surface of TGE (1% tryptone, 1% glucose and 1% yeast extract, pH 6.5) agar plates with sterile cotton swabs. Then, 10 μL of the sample solution in sterile distilled water containing 100 mg mL^{-1} concentration was spotted on the plate along with the antibiotic spot. The plates were then incubated at 37 °C for 24 hours. The experiment was carried out in triplicate.

3. Results and discussion

3.1. Rheological analysis

To assess the mechanical strength and viscoelastic properties of the NiC-GT metallohydrogel, rheological studies were conducted using a rheometer. Measurements included both angular frequency sweep and strain sweep tests, performed on a sample prepared at the minimum gelation concentration (MGC) of 355 mg mL^{-1} using $NiCl_2 \cdot 6H_2O$ and guanylthiourea. The material's gel-like behaviour was evident from the predominance of the storage modulus (G′) over the loss modulus (G″), indicating its elastic and semi-solid nature. Notably, G′ remained substantially higher than G″ throughout the frequency range, confirming the viscoelastic character of the hydrogel (Fig. 2a). The average storage modulus (G′) exceeded 10^4 Pa, pointing to a mechanically robust network stabilized through coordination between Ni(II) ions and guanylthiourea, along with various non-covalent interactions. Additionally,

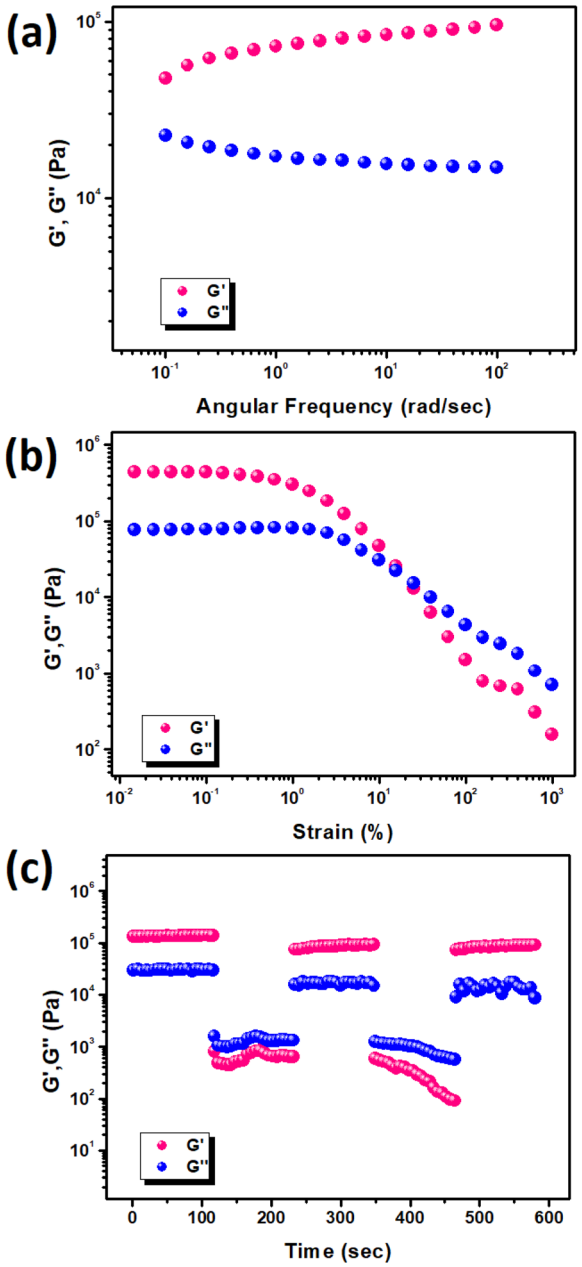

Fig. 2 (a) Angular frequency measurements *vs.* G' and G'' of NiC-GT metallohydrogel; (b) strain-sweep measurements of NiC-GT metallohydrogel performed at a constant frequency of 6.283 rad s; (c) thixotropic measurement performed on the NiC-GT metallohydrogel, examining its thixotropic behavior.

strain sweep tests conducted at a constant angular frequency of 6.283 rad s^{-1} revealed the gel's ability to maintain its structural integrity under increasing strain levels (Fig. 2b). The material withstood deformation over a wide strain range before yielding, highlighting its excellent strain resistance. These results underscore the strong mechanical stability of the NiC-GT metallohydrogel, supporting its potential for applications in soft materials and flexible electronic technologies.

However, it's worth noting that the storage modulus (G') exceeded the loss modulus (G'') until the strain reached approximately 0.1%, indicating a transition from gel to sol. To investigate the self-healing behavior, a thixotropy test was conducted (Fig. 2c). Interestingly, the soft material remained in the gel state at a strain of about 0.01% but rapidly transformed into a sol state when the strain was abruptly increased to around 100%. Upon reducing the high strain, the soft material quickly reverted to a viscoelastic gel state. This cyclic transition between low and high strain confirmed the reversible transformation of the soft material from a gel to a sol state. Such behavior is highly desirable for applications requiring repeated mechanical stress, as it ensures the metallohydrogel's stability, reusability, and mechanical reliability.

3.2. Study of morphology

Field emission scanning electron microscopy (FESEM) analysis of the NiC-GT metallohydrogel demonstrates a distinctly

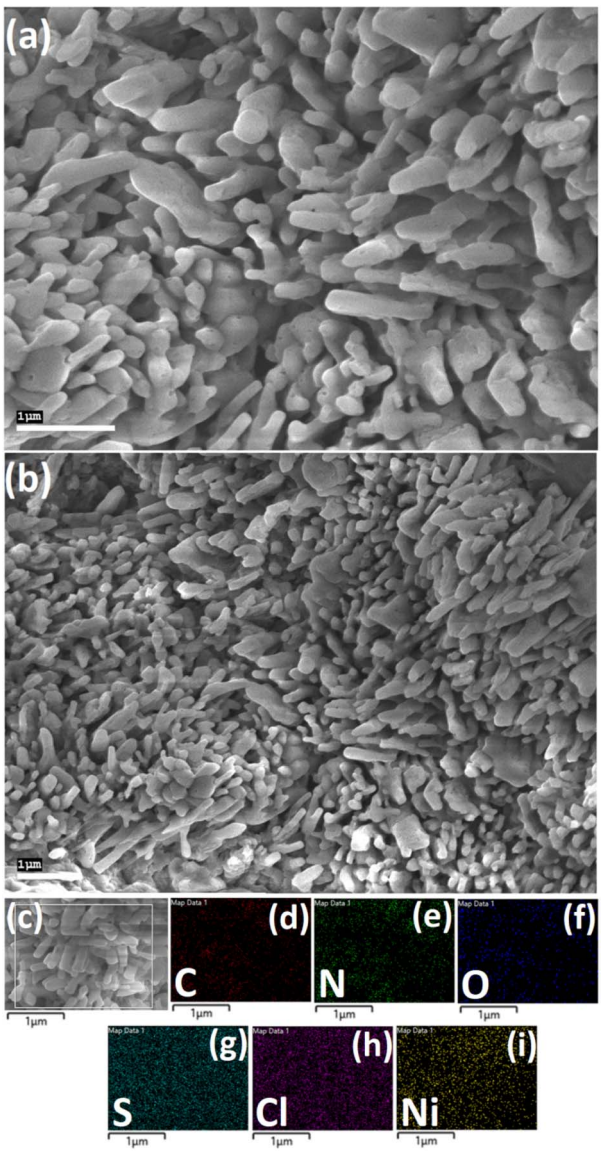

Fig. 3 (a and b) FESEM analysis reveals the microstructural features of the NiC-GT metallohydrogel, (c–i) the elemental mapping of NiC-GT metallohydrogel showing the presence of C, N, O, S, Cl and Ni elements.

organized, hierarchical fibrous network (Fig. 3a and b). This structural arrangement originates from the coordination between $NiCl_2 \cdot 6H_2O$ and guanylthiourea in an aqueous environment. The formation of such a network is driven by robust supramolecular interactions, which are essential for maintaining the stability of the gel architecture. Elemental mapping of a selected region confirms the homogeneous distribution of essential components, including nickel and guanylthiourea. Complementary energy-dispersive X-ray spectroscopy (EDX) analysis detects the presence of carbon (C), nitrogen (N), oxygen (O), sulfur (S), chlorine (Cl), and nickel (Ni), reinforcing the successful integration of these elements within gel matrix (Fig. 3c–i). Together, these observations affirm the formation of a stable and compositionally uniform supramolecular network, emphasizing the gel's structural coherence and integrity.

3.3. FT-IR analysis of NiC-GT metallohydrogel

Fourier Transform Infrared (FT-IR) spectroscopy is a vital analytical tool for identifying functional groups and understanding molecular interactions within metallohydrogels. The FT-IR spectrum of NiC-GT metallohydrogel distinctly reflects the presence of its key components through the major characteristic absorption bands at 600, 639, 667, 730, 810, 976, 999, 1096, 1134, 1307, 1371, 1415, 1489, 1582, 1626 and 1671 (Fig. 4). The spectrum exhibits notable peak shifts at 810 cm^{-1}, 1096 cm^{-1} and 1415 cm^{-1}, which are characteristic of nickel chloride.

Additionally, distinct absorption bands at 639 cm^{-1}, 667 cm^{-1}, 976 cm^{-1}, 999 cm^{-1}, 1134 cm^{-1} and 1307 cm^{-1} further validate the incorporation of guanylthiourea within the metallohydrogel network. The combination of these spectral features provides crucial insights into the structural composition of the NiC-GT metallohydrogel, confirming the successful integration of its key components (Fig. 4).

The spectral region between 3450 and 3100 cm^{-1} is associated[55,56] with both asymmetric and symmetric NH_2^+ stretching vibrations. Within this range, symmetric N–H stretching is specifically detected between 3100 and 3300 cm^{-1}. A distinct band appearing at 1669 cm^{-1} results from a combination of C–N and C=N stretching vibrations[55,56] along with NH_2 bending modes. Additionally, NH_2^+ deformation vibrations are typically observed[55] between 1660–1610 cm^{-1} for asymmetric modes and 1550–1485 cm^{-1} for symmetric modes.

In the present study, characteristic N–H stretching frequencies are identified at 3451, 3420, 3340, and 3221 cm^{-1}, indicating the presence of key functional groups. Among these, the first two bands correspond[52] to asymmetric stretching, while the latter two represent symmetric vibrations. Interestingly, the final peak appear at lower frequencies than expected, likely due[55] to the influence of sulfur within the molecular framework. In-plane N–H bending vibrations are typically found between 1610–1630 cm^{-1}, while rocking motions are detected within the 1100–1200 cm^{-1} range. Similarly, out-of-plane bending vibrations (wagging and twisting) are generally observed between 900 and 1150 cm^{-1} (Fig. 4).

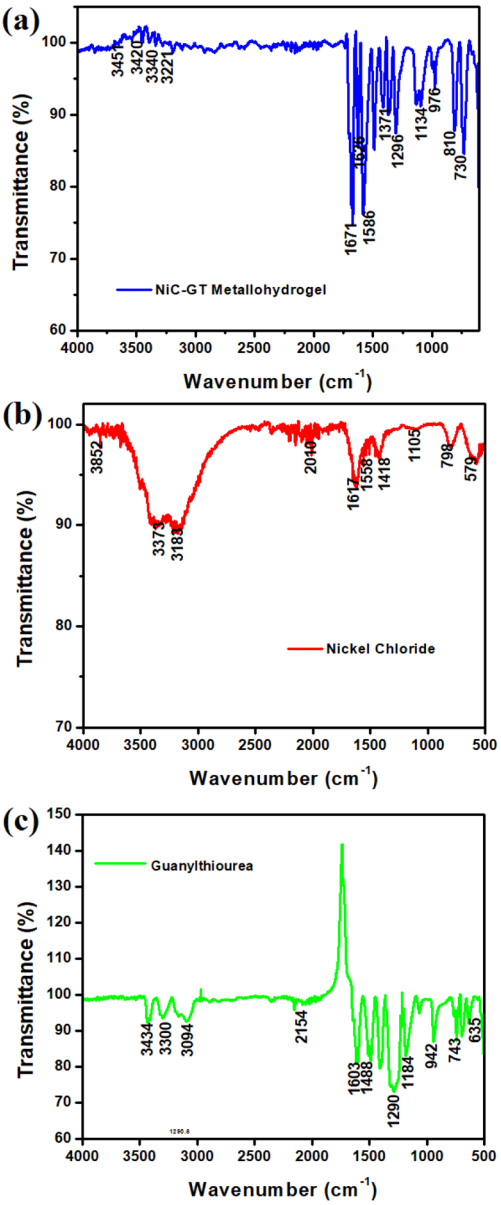

Fig. 4 (a–c) FT-IR spectra of the xerogel form of NiC-GT metallohydrogel, nickel chloride hexahydrate salt and guanylthiourea gelator.

Previous studies, such as those by Silverstein,[57] have reported C–N stretching vibrations in the 1386–1266 cm^{-1} range for aromatic amines. However, in this case, the C–N stretching bands appear at 1096, 1000, and 720 cm^{-1}, which deviates from the literature. This shift may be attributed[55] to the incorporation of sulfur and metal atoms within the molecular structure. The mode of bonding can be distinguished by examining C–S stretching vibrations, which occur at 730–690 cm^{-1} when bonded through sulfur and within 860–780 cm^{-1} when bonding occurs *via* nitrogen (Fig. 4).

In metal complexes, Ni–Cl stretching vibrations are a notable feature, typically appearing[55] between 525 and 220 cm^{-1}. In this system, the organic compound is coordinated[55] to metal chloride *via* sulfur atoms, forming an S–Ni–S bridge through

a coordinate covalent bond. Due to strong organic vibrational influences, Ni–S stretching vibrations are often overshadowed by larger force constants and stronger covalent interactions. As a result, the weak Ni–S coordinate bond causes its vibrations to merge with those of Ni–Cl, shifting them to the lower end of the IR spectrum, indicating a relatively weak interaction between the metal and the organic ligand (Fig. 4).

3.4. PXRD analysis of NiC-GT metallohydrogel

A Powder X-ray Diffraction (PXRD) analysis was conducted to thoroughly investigate the structural organization of the metallohydrogel and assess the presence of any crystalline phases. This analytical technique is extensively utilized to investigate the molecular arrangement and phase composition of materials by examining the interaction of X-rays with the atomic structure of the sample. In this study, the PXRD pattern of the metallohydrogel was recorded over a wide angular range, extending from 5° to 80°, to gather detailed structural information. The diffraction pattern, as depicted in Fig. 5, offers valuable insights into the material's crystallinity. By analyzing the characteristic diffraction peaks and their intensities, the structural framework of the metallohydrogel can be elucidated, providing crucial information regarding its molecular interactions and overall organization.

The crystallinity of the NiC-GT metallohydrogel is distinctly reflected in the sharp diffraction peaks observed at 2θ values of 5.9°, 7.26°, 11.52°, 19.54°, 22.3°, 24.6°, 26.6°, 30.6°, 38.3°, and 43.04°. These well-defined peaks indicate a highly ordered structure within the gel network. Among these, the peaks at 16°, 19°, 26°, 31°, 45°, and 53° are characteristic of nickel chloride, aligning closely with previously reported diffraction patterns,[58] confirming the presence of this component in the metallohydrogel matrix. Additionally, diffraction peaks corresponding to guanylthiourea are observed at 15.7°, 17.6°,26.5°, 29.7°, 30.7°, 34.1°,39.3°, 40.3°[59] reinforcing the structural framework of the metallohydrogel and suggesting that this organic component plays a role in the overall organization of the system (Fig. 5). The observed shifts in peak positions suggest that subtle changes occur in the molecular arrangement during gelation, potentially due to the dynamic interactions between metal ions and organic ligands as the gel network forms and stabilize. These structural transformations likely arise from the self-assembly processes governing the gelation, where intermolecular forces, hydrogen bonding, and coordination interactions contribute to the final organization of the NiC-GT metallohydrogel.

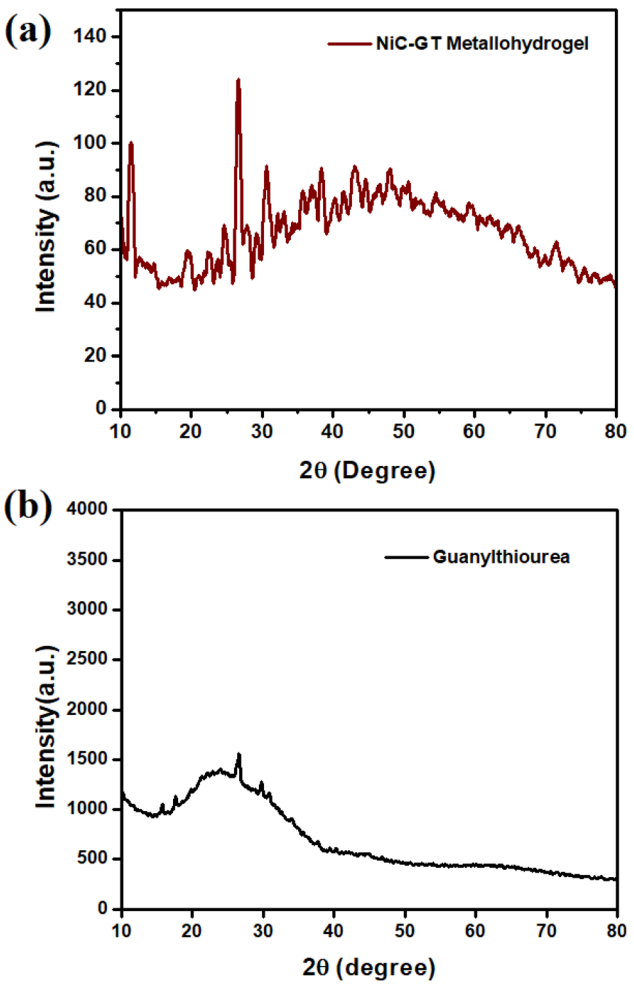

Fig. 5 (a and b) PXRD pattern of the NiC-GT metallohydrogel and guanylthiourea.

3.5. Fabrication and electrical characterization of thin film device

Forming a continuous thin film of NiC-GT metallohydrogel on conductive substrates such as Indium Tin Oxide (ITO) is essential for exploring its potential in semiconductor devices, particularly for applications that require efficient charge transport. However, the gel's inherent viscoelastic properties present a significant challenge in achieving a smooth and uniform coating. This can lead to inconsistent films, compromising both the electrical performance and structural integrity. To resolve this, polymethylmethacrylate (PMMA) is incorporated as a structural support, which helps disperse the NiC-GT metallohydrogel in *N*,*N*-dimethylformamide (DMF) and improves its ability to form uniform films. The device fabrication requires fine, uniform and pin-hole free films of the gel. Due to the gel characteristics and heavy dispersion particles in solution, forming such fine thin films of these gels are extremely difficult. Therefore, as is the practice, an appropriate polymer maybe used as a binder material to spread the dispersed particles of the gel in solution leading to a fine film on spin coating. Polymethylmethacrylate (PMMA, an insulating polymer), is employed here as a matrix and binder to achieve a fine dispersion of the gel in DMF. PMMA was selected here due to its already known excellent film-forming ability, mechanical stability, and optical transparency.[60,61] Its high adhesion strength enables the formation of uniform, defect-free thin films, which is essential for ensuring consistent contact between the metallohydrogel and the substrate.[60–62] PMMA is chemically stable, resistant to moisture, and compatible with a wide range of solvents[60,63] used in metallohydrogel

preparation, preventing degradation or unwanted reactions during synthesis.

The preparation process begins by dissolving PMMA in DMF at 40 °C while stirring continuously for two hours. This ensures the PMMA is fully dissolved and evenly distributed in the solvent. Subsequently, various concentrations of PMMA ranging from 10 to 50 weight percentages are added to the NiC-GT metallohydrogel. The mixture is stirred for an additional four hours to ensure complete integration. The resulting films are analyzed for uniformity, adhesion, and coverage on the ITO substrate. Among the different formulations, the addition of 50 weight percentage PMMA yielded the most homogeneous and smooth films, providing excellent substrate coverage with minimal surface irregularities.

Beyond this concentration, increasing the amount of PMMA leads to diminishing returns. Higher concentrations result in structural instability, poor adhesion to the substrate, and a noticeable degradation in film quality. This underscores the importance of fine-tuning the PMMA concentration to achieve optimal film formation. The presence of PMMA not only enhances the gel's ability to form uniform films but also contributes to the overall stability and electrical performance of the NiC-GT metallohydrogel when used in semiconductor devices. Therefore, the careful balance between PMMA content and gel properties is critical for optimizing thin film fabrication for electronic applications.

Before deposition, the ITO glass substrates undergo an extensive cleaning process to remove any contaminants, dust, or organic residues that might hinder the uniformity and adhesion of the thin films. This cleaning is crucial for ensuring that the surface is free from impurities that could negatively impact the subsequent film formation or the electrical properties of the device. Once cleaned, the substrates are ready for the deposition of the NiC-GT-PMMA blend. The NiC-GT-PMMA mixture is uniformly spread over the substrate using spin-coating at 1000 rpm for 50 seconds. Spin-coating is an efficient method that ensures the film is evenly distributed across the substrate, achieving the desired thickness and uniformity. Following this step, the coated substrate undergoes an annealing process at 60 °C for five minutes. The annealing helps to further stabilize the film, enhancing its structural integrity and improving the overall quality of the coating. This heat treatment also assists in the evaporation of any residual solvent, ensuring that the film is solidified and prepared for the subsequent layers.

After the NiC-GT-PMMA film is prepared, a thin layer of aluminum, approximately 100 nm thick, is deposited on top of the NiC-GT-PMMA layer through vacuum evaporation. This technique allows for the precise deposition of metal, ensuring a smooth and well-controlled aluminum layer. The resulting structure forms a layered configuration of ITO/NiC-GT-PMMA/Al, which is essential for the formation of the complete device. The aluminum layer plays a crucial role in ensuring good electrical contact with the underlying NiC-GT metallohydrogel, facilitating charge transport within the device.

To evaluate the electrical behavior of the fabricated thin film device, current–voltage (I–V) measurements are carried out using a Keithley 2450 source meter. A bias voltage is applied to the device within the range of 0 to ±2 V to assess the electrical response under different applied voltages. These measurements provide important data regarding the charge transport properties, including the device's conductivity and overall performance. The resulting I–V characteristics, which are shown in Fig. 6, offer a detailed view of the electrical behavior of the device, allowing for further analysis of its suitability for use in semiconductor applications. The I–V curve provides valuable insights into the device's functionality, revealing how the thin film responds to changes in applied voltage, which is critical for determining its efficiency and potential in practical applications.

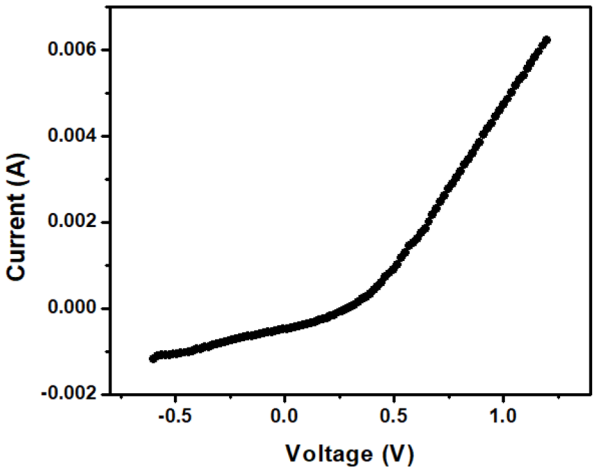

Fig. 6 I–V characteristics of NiC-GT metallohydrogel based diode.

The electrical performance of the NiC-GT metallohydrogel-based device reveals current–voltage (I–V) characteristics akin to those observed in Schottky diodes. To gain deeper insights into its charge transport mechanisms, the I–V response is evaluated using Thermionic Emission theory, which provides a fundamental framework for understanding carrier movement across the junction. Additionally, key diode parameters, such as the ideality factor and barrier height, are extracted through Cheung's method,[64] a widely used analytical approach for assessing semiconductor interfaces. The mathematical expressions governing these phenomena are outlined below, offering a quantitative basis for interpreting the observed behaviour.

$$I = I_0\left(\frac{qV}{\eta KT}\right)\left[1 - \exp\left(\frac{-qV}{\eta KT}\right)\right] \quad (1)$$

$$I_0 = AA^*T^2\exp\left(\frac{-q\varphi_B}{\eta KT}\right) \quad (2)$$

In this analysis, the applied bias voltage is represented by V, while k denotes the Boltzmann constant, and q is the elementary charge of an electron. The temperature, expressed in Kelvin as T, plays a crucial role in governing carrier dynamics, and the reverse saturation current is given by I_0. The device's effective diode area is denoted by A, with the Richardson constant A^* assumed to be 32 A K^{-2} cm^{-2}.

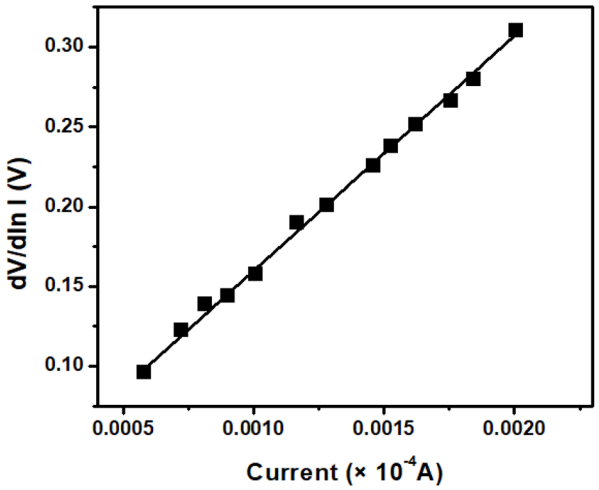

Fig. 7 $\frac{dV}{d(\ln I)}$ *vs. I* plot of NiC-GT metallohydrogel based Schottky diode.

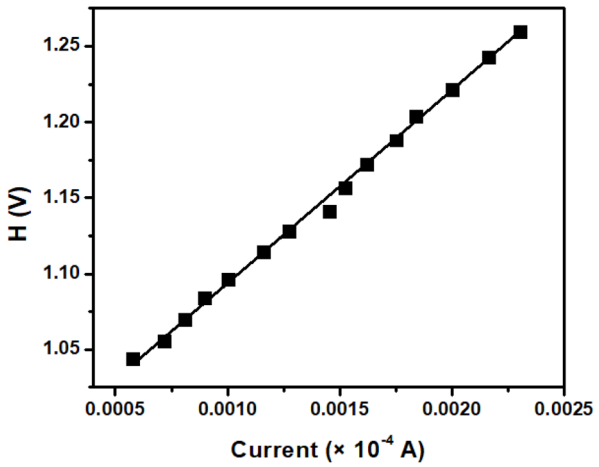

Fig. 8 *H vs. I* plot of NiC-GT metallohydrogel based Schottky diode.

To extract essential diode parameters including the ideality factor (n), barrier height (φ_B), and series resistance (R_s), Cheung's method is employed.[64] This approach focuses on analyzing the *I–V* characteristics and utilizes differential techniques to linearize the inherently nonlinear diode response, enabling precise parameter determination. The series resistance is obtained from the slope of the modified function dV/d ln$I$ plotted against current (as illustrated in Fig. 7). Once these parameters are extracted, the barrier height is determined by integrating them into the thermionic emission framework. The fundamental equations relevant to these calculations are detailed below.

$$\frac{dV}{d(\ln I)} = \left(\frac{\eta KT}{q}\right) + IR_s \quad (3)$$

$$H(I) = V - \left(\frac{\eta KT}{q}\right)\ln\left(\frac{I}{AA^*T^2}\right) \quad (4)$$

Fig. 8 provides a graphical representation of the $H(I)$ *versus* I plot, a critical tool in evaluating the barrier height (φ_B) of the diode. This plot is constructed based on the previously discussed equations, allowing for a systematic approach to parameter extraction. The slope and intercept of this plot, when analyzed alongside the ideality factor (n), enable a precise determination of (φ_B), offering valuable insight into the charge transport characteristics of the device. By leveraging this method, the complex nonlinear behavior of the diode can be effectively linearized, facilitating a more accurate estimation of key electronic properties. This approach not only enhances the reliability of barrier height calculations but also contributes to a deeper understanding of the underlying mechanisms governing carrier dynamics in the system.

Table 1 presents the estimated values of key electrical parameters that characterize the NiC-GT metallohydrogel's device performance. These include the ON/OFF ratio, which reflects the switching capability of the device, and the conductivity, which provides insight into charge transport efficiency. Additionally, the table lists the ideality factor (n), a crucial parameter that indicates the deviation of the diode from ideal behavior, as well as the barrier potential (φ_B), which influences charge carrier injection across the junction. The series resistance (R_s) is also included, as it affects the overall current flow and device efficiency. Together, these parameters offer a comprehensive understanding of the NiC-GT metallohydrogel's electronic properties and its potential applications in various device architectures.

The functional supramolecular Ni(II)-metallohydrogel used here is synthesized using guanylthiourea, a low molecular weight gelator (LMWG). As a low molecular weight gelator with efficient metal ion chelation, it provides a soft scaffold for electron transfer. This soft scaffold may be facilitating the necessary electron transportation needed for the semiconducting action of the gel in the device structure presented here. In this investigation, the mobility of charge carriers was evaluated through the application of the widely recognized

Table 1 Key Electrical parameters of the NiC-GT metallohydrogel based schottky diode-ON/OFF ratio, conductivity, ideality factor, barrier potential, and series resistance

			Series resistance (Ω)		
Conductivity (S m^{-1})	Ideality factor	Barrier height (eV)	dV/d ln I *vs.* I graph	H *vs.* I graph	Mobility (cm^2 V^{-1} s^{-1})
1.85	1.22	0.79	127.22	117.29	2.31×10^{-2}

Table 2 Comparison table of electrical parameters of NiC-GT metallohydrogel based device with other reported results

Sample name	Rectification ratio	Electrical conductivity (S m^{-1})	Barrier height (eV)	Ideality factor	Ref.
Ni@5AIA	34.77	1.53×10^{-5}	0.68	3.18	39
Zn@TA	37.06	7.77×10^{-5}	0.47	3.78	66
Fe-metallogel	42.19	4.53×10^{-6}	0.78	2.92	67
Mn@OX	—	1.27×10^{-4}	0.22	2.19	20
CdA-OX	—	5.35×10^{-4}	0.32	1.8	15
Mg@MEA	—	1.43×10^{-5}	0.38	1.89	68
MnA-TA	41.85	2.16×10^{-5}	0.48	1.47	29
ZnA-TA	64.99	4.45×10^{-5}	0.39	1.21	29
Cd-AIA	—	1.27×10^{-2}	0.705	6.80	45
Hg-AIA	—	1.9×10^{-1}	0.626	4.49	45
NiC-GT	—	1.85	0.79	1.22	This work

Mott–Gurney equation,[65] a fundamental model extensively utilized for analyzing space-charge-limited current (SCLC) behavior in both organic materials and semiconductor-based systems. This approach provides a reliable means of understanding charge transport mechanisms by describing how carriers move under high-injection conditions, where space-charge effects become dominant. By leveraging this theoretical framework, valuable insights can be gained into the electrical properties of the material, enabling a deeper comprehension of its conduction characteristics and potential applicability in various electronic and optoelectronic devices.

$$I = \frac{9}{8}\varepsilon_r \varepsilon_0 \mu A \frac{V^2}{d^3} \quad (5)$$

In this formulation, ε_0 represents the permittivity of free space, while ε_r signifies the dielectric constant specific to the material blend. The charge carrier mobility is denoted by μ, a crucial parameter that influences the overall charge transport dynamics. Additionally, d corresponds to the thickness of the film, which plays a significant role in determining the device's electrical characteristics by affecting the space-charge-limited conduction behavior.

The NiC-GT sample developed in this work exhibits the highest electrical conductivity (1.85 S m^{-1}), far surpassing all reported metallohydrogels, indicating superior charge transport capability. While several materials such as ZnA-TA and MnA-TA show good rectification ratios, NiC-GT combines high conductivity with a moderate barrier height (0.79 eV) and a low ideality factor (1.22), suggesting efficient and near-ideal diode behaviour. This performance highlights its strong potential for high-performance electronic and optoelectronic device applications. The comparison table is shown below (Table 2).

The morphological aspects as evidenced by the FESEM micrographs clearly indicate the immediate semiconducting behavior of the gel. Images in Fig. 3 provide a lucid and vivid picture of vertically oriented rod-type microstructure of the gel films. In the diode device structure used here, the gel layer is sandwiched between the electrodes. The observed semiconducting behavior of the gel layer in the vertically oriented device can be traced to the presence of highly conducting elements, carbon and Ni, in the evenly dispersed and vertically oriented rod-type microstructure.

To indicate the semiconductor device application potential of the gel, we used a diode device architecture with the gel film as the semiconductor and ITO and aluminum as the sandwiching electrodes. As discussed in the relevant section, the current–voltage characteristics of the device exhibited a fairly good semiconductor nature. We were not able to evaluate the conductivity values or their variation with temperature due to the lack of availability of experimental facility for conductivity measurements, as the conductivity of such semiconductors are in the range of that typically shown by organic semiconductors, and high resistivity meters are essentially required. However, the diode characteristics presented here points to the strong potential of the gel to be used in semiconductor device applications.

3.6. Inhibiting activity for pathogens

The incorporation of metal components into gel matrices may be a possible alternative to antibiotics in the scenario of antibiotic resistance due to their enhanced antimicrobial activity.

Table 3 Activity of positive control (antibiotic streptomycin) against bacterial strain(s)

Bacterial strain (s)	Volume of antibiotic given as positive control (μL)	Concentration of antibiotic used as positive control (mg mL^{-1})	Zone of inhibition (mm in diameter)
Escherichia coli	5	1	12 ± 0.15
Bacillus subtilis	5	1	21 ± 0.12
Pseudomonas aeruginosa	5	1	15 ± 0.2
Staphylococcus aureus	5	1	18 ± 0.1

Table 4 Activity of sample NiC-GT against bacterial strain(s)

Bacterial strain (s)	Volume of sample given (μL)	Concentration of sample solution (mg mL^{-1})	Zone of inhibition (mm in diameter)
Escherichia coli	10	100	14 ± 0.18
Bacillus subtilis	10	100	No zone
Pseudomonas aeruginosa	10	100	17 ± 0.2
Staphylococcus aureus	10	100	16 ± 0.12

Metallohydrogels show potential antibacterial activity through multiple mechanisms. One critical pathway involves the slow release of metal ions from the gel matrix. These ions penetrate the bacterial cell wall and later interfere with protein and DNA function. Moreover, certain metal ions catalyze reactive oxygen species (ROS) production, causing oxidative damage to proteins, lipids, and nucleic acids, leading to cell death.[69] Our present study evaluates the antimicrobial potential of synthesized NiC-GT metallohydrogel against both Gram-positive and Gram-negative bacterial strains with antibiotic streptomycin as positive control (Table 3). Due to incubation, the metallohydrogels diffuse into the growth medium, resulting a circular clear region where the metallohydrogel concentration is inhibitory to bacterial growth, called the zone of inhibition. The size of these clear zones corresponds to the efficacy of the metallohydrogel against the tested organisms. The results demonstrate that NiC-GT metallohydrogel possesses considerable antibacterial activity, particularly against Gram-negative bacteria *Escherichia coli*, *Pseudomonas aeruginosa*, and Gram-positive bacteria *Staphylococcus aureus,* with significant inhibition zones (Table 4). Among the bacterial strains, *Bacillus subtilis* exhibited no inhibition zone in the presence of NiC-GT metallohydrogel, despite being highly sensitive to streptomycin. This suggests a degree of selectivity or reduced permeability of the metallohydrogel to certain Gram-positive bacteria, which may be attributed to differences in cell wall structure or interactions between the gel matrix and bacterial surface components. Conversely, the inhibition of *Pseudomonas aeruginosa*-a pathogen known for its intrinsic resistance to many antibiotics-is particularly significant, emphasizing the potential of NiC-GT metallohydrogel as an alternative to common antimicrobial materials (Fig. 9). A comparative evaluation with previously reported metallohydrogels suggests that Ni(II) system is significantly promising. For example, suberic acid-based Cd(II), Zn(II), and Ni(II) metallohydrogels reported by *Lepcha et al.* revealed selective bactericidal activity, with Cd-SA being the most potent overall, but Ni-SA performed well against certain Gram-negative strains such as *Klebsiella pneumoniae* and *Salmonella typhi*.[70] Furthermore, squaric acid-mediated Zn(II) and Cd(II) metallogels have shown considerable potency against ESKAPE pathogens,[71] though concerns regarding metal toxicity remain a limiting factor for their biomedical translation. We could not investigate the dependence of the semiconductor or antibacterial property on environmental conditions due to our limitations with experimental facilities to effects such as the change of conductivity and the attenuation of antibacterial effect.

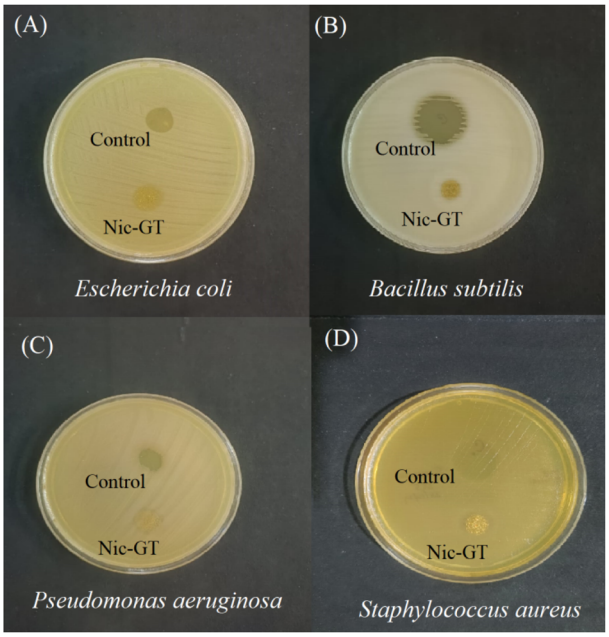

Fig. 9 Antibacterial activity of sample NiC-GT against (A) *Escherichia coli* (B) *Bacillus subtilis* (C) *Pseudomonas aeruginosa* (D) *Staphylococcus aureus*. Antibiotic streptomycin was used as positive control.

4. Conclusions

In this study, we present the efficient fabrication of a supramolecular Ni(II)-based metallohydrogel by simply mixing nickel chloride hexahydrate with guanylthiourea in water at room temperature. The process yielded a stable gel within a short time, highlighting the simplicity and scalability of the method. Field emission scanning electron microscopy (FESEM) revealed an organized fibrous and hierarchical microstructure, while rheological evaluations demonstrated the gel's significant mechanical strength. Fourier-transform infrared (FT-IR) spectroscopy confirmed the presence of key non-covalent interactions that play a major role in the gelation process. Powder X-ray diffraction (PXRD) analysis further indicated the semi-crystalline nature of the NiC-GT metallohydrogel. Optical band-gap analysis confirmed its semiconducting properties, which were validated by incorporating the gel into an ITO/NiC-GT-PMMA/Al thin-film diode device-exhibiting clear rectifying behavior, making it suitable for optoelectronic applications. Additionally, the metallohydrogel showed strong antibacterial efficacy against *Escherichia coli, Bacillus subtilis, Pseudomonas*

aeruginosa and *Staphylococcus aureus*, with activity comparable to the standard antibiotic streptomycin. This environmentally friendly and straightforward approach paves the way for the development of multifunctional soft materials, offering promising potential in biomedical, environmental, and flexible electronic applications. The findings emphasize the utility of rational supramolecular design for next-generation functional hydrogels.

Conflicts of interest

The authors declare no competing financial interests.

Data availability

The authors declare that all data related to this study are included in the paper. Any raw data files required in a different format can be obtained from the corresponding author upon reasonable request.

Acknowledgements

S. S. is thankful to DST India, New Delhi for Inspire Fellowship (No. DST/inspire Fellowship/2022/IF220441). S. B. thankfully acknowledges DST Inspire Faculty Research Grant (Faculty Registration No. IFA18-CH304; DST/INSPIRE/04/2018/000329).

Notes and references

1 D. Tripathy, A. S. Gadtya and S. Moharana, *Polym.-Plast. Technol. Mater.*, 2023, **62**, 306–326.
2 S. Datta and S. Bhattacharya, *Chem. Soc. Rev.*, 2015, **44**, 5596–5637.
3 A. Pape, M. Bastings, R. Kieltyka, H. Wyss, I. Voets, E. Meijer and P. Dankers, *Int. J. Mol. Sci.*, 2014, **15**, 1096–1111.
4 S. Dhibar, H. Dahiya, K. Karmakar, S. Kundu, S. Bhattacharjee, G. C. Nayak, P. Karmakar, G. D. Sharma and B. Saha, *J. Mol. Liq.*, 2023, **370**, 121020.
5 K. Karmakar, A. Dey, S. Dhibar, R. Sahu, S. Bhattacharjee, P. Karmakar, P. Chatterjee, A. Mondal and B. Saha, *RSC Adv.*, 2023, **13**, 2561–2569.
6 S. Ganta and D. K. Chand, *Dalton Trans.*, 2015, **44**, 15181–15188.
7 G. Yu, X. Yan, C. Han and F. Huang, *Chem. Soc. Rev.*, 2013, **42**, 6697.
8 S. Dhibar, A. Dey, S. Majumdar, A. Dey, P. P. Ray and B. Dey, *Ind. Eng. Chem. Res.*, 2020, **59**, 5466–5473.
9 M. Shirakawa, N. Fujita and S. Shinkai, *J. Am. Chem. Soc.*, 2003, **125**, 9902–9903.
10 T.-A. Asoh and A. Kikuchi, *Chem. Commun.*, 2012, **48**, 10019.
11 X. Yang, H. Zhang, J. Zhao, Y. Liu, Z. Zhang, Y. Liu and X. Yan, *Chem. Eng. J.*, 2022, **450**, 138135.
12 A. Rajak and A. Das, *ACS Polymers Au*, 2022, **2**, 223–231.
13 Y. Xu, Q. Wu, Y. Sun, H. Bai and G. Shi, *ACS Nano*, 2010, **4**, 7358–7362.
14 J. W. Steed, *Chem. Soc. Rev.*, 2010, **39**, 3686.
15 S. Dhibar, A. Dey, S. Majumdar, D. Ghosh, A. Mandal, P. P. Ray and B. Dey, *Dalton Trans.*, 2018, **47**, 17412–17420.
16 K. Hanabusa, K. Hiratsuka, M. Kimura and H. Shirai, *Chem. Mater.*, 1999, **11**, 649–655.
17 A. Prathap and K. M. Sureshan, *Langmuir*, 2019, **35**, 6005–6014.
18 S. Dhibar, A. Dey, D. Ghosh, S. Majumdar, A. Dey, P. P. Ray and B. Dey, *ACS Omega*, 2020, **5**, 2680–2689.
19 S. Dhibar, A. Dey, R. Jana, A. Chatterjee, G. K. Das, P. P. Ray and B. Dey, *Dalton Trans.*, 2019, **48**, 17388–17394.
20 S. Dhibar, A. Roy, P. Das, T. Sarkar, M. Goswami, S. Some, K. Karmakar, P. Ruidas, S. Bhattacharjee, T. O Ajiboye, A. S. Ray, K. Sarkar, S. J. Ray and B. Saha, *Mater. Adv.*, 2025, **6**, 1899–1913.
21 A. Roy, S. Dhibar, K. Karmakar, S. Bhattacharjee, B. Saha and S. J. Ray, *Sci. Rep.*, 2024, **14**, 13109.
22 S. Dhibar, A. Roy, T. Sarkar, P. Das, K. Karmakar, S. Bhattacharjee, B. Mondal, P. Chatterjee, K. Sarkar, S. J. Ray and B. Saha, *Langmuir*, 2024, **40**, 179–192.
23 K. Karmakar, A. Roy, S. Dhibar, S. Majumder, S. Bhattacharjee, B. Mondal, S. M. Rahaman, R. Saha, S. J. Ray and B. Saha, *ACS Appl. Electron. Mater.*, 2023, **5**(6), 3340–3349.
24 M.-O. M. Piepenbrock, G. O. Lloyd, N. Clarke and J. W. Steed, *Chem. Rev.*, 2010, **110**, 1960–2004.
25 S. Dhibar, A. Dey, A. Dalal, S. Bhattacharjee, R. Sahu, R. Sahoo, A. Mondal, S. M. Rahaman, S. Kundu and B. Saha, *J. Mol. Liq.*, 2023, **370**, 121021.
26 S. Dhibar, S. Babu, A. Mohan, G. K. Chandra, S. Bhattacharjee, K. Karmakar, P. Karmakar, S. M. Rahaman, P. Predeep and B. Saha, *J. Mol. Liq.*, 2023, **375**, 121348.
27 S. Dhibar, B. Pal, K. Karmakar, S. Kundu, S. Bhattacharjee, R. Sahoo, S. M. Rahaman, D. Dey, P. P. Ray and B. Saha, *ChemistrySelect*, 2023, **8**, e202204214.
28 S. Dhibar, B. Pal, K. Karmakar, S. Roy, S. A. Hafiz, A. Roy, S. Bhattacharjee, S. J. Ray, P. P. Ray and B. Saha, *Nanoscale Adv.*, 2023, **5**, 6714–6723.
29 S. Dhibar, A. Dey, B. Mondal, K. Karmakar, A. Roy, S. Bhattacharjee, A. Trivedi, A. Mohan, R. Saha, P. Chatterjee, A. Mondal, T. O Ajiboye and B. Saha, *J. Sol-Gel Sci. Technol.*, 2025, **113**, 896–909.
30 S. Dhibar, A. Mohan, K. Karmakar, B. Mondal, A. Roy, S. Babu, P. Garg, P. Ruidas, S. Bhattacharjee, S. Roy, A. Bera, S. J. Ray, P. Predeep and B. Saha, *RSC Adv.*, 2024, **14**, 12829–12840.
31 A. Roy, S. Dhibar, S. Kumar, S. Some, P. Garg, P. Ruidas, S. Bhattacharjee, A. Bera, B. Saha and S. J. Ray, *Sci. Rep.*, 2024, **14**, 31619.
32 A. Roy, S. Dhibar, S. Kumar, K. Karmakar, P. Garg, P. Ruidas, S. Bhattacharjee, A. Bera, B. Saha and S. J. Ray, *Sci. Rep.*, 2024, **14**, 26848.
33 S. Ganta and D. K. Chand, *Dalton Trans.*, 2015, **44**, 15181–15188.
34 C. Po, Z. Ke, A. Y. Tam, H. Chow and V. W. Yam, *Chem.–Eur. J.*, 2013, **19**, 15735–15744.

35 B. Jiang, L.-J. Chen, G.-Q. Yin, Y.-X. Wang, W. Zheng, L. Xu and H.-B. Yang, *Chem. Commun.*, 2017, **53**, 172–175.
36 S. Dhibar, A. Dey, A. Dey, S. Majumdar, D. Ghosh, P. P. Ray and B. Dey, *ACS Appl. Electron. Mater.*, 2019, **1**, 1899–1908.
37 S. Dhibar, S. K. Ojha, A. Mohan, S. P. C. Prabhakaran, S. Bhattacharjee, K. Karmakar, P. Karmakar, P. Predeep, A. K. Ojha and B. Saha, *New J. Chem.*, 2022, **46**, 17189–17200.
38 B. Pal, S. Dhibar, R. Mukherjee, S. Bhattacharjee, P. P. Ray and B. Saha, *Mater. Adv.*, 2023, **4**, 3628–3635.
39 S. Dhibar, S. K. Ojha, K. Karmakar, P. Karmakar, S. Bhattacharjee, P. Chatterjee, A. K. Ojha and B. Saha, *Chemistry*, 2023, **6**, 3217–3228.
40 S. Dhibar, S. Babu, K. Karmakar, A. Mohan, S. Bhattacharjee, S. M. Rahaman, G. C. Nayak, R. Saha, P. Predeep and B. Saha, *Chem. Phys. Lett.*, 2023, **829**, 140777.
41 A. Roy, S. Dhibar, K. Karmakar, S. Some, S. A. Hafiz, S. Bhattacharjee, B. Saha and S. J. Ray, *Mater. Adv.*, 2024, **5**, 3459–3471.
42 J. Chen, T. Wang and M. Liu, *Inorg. Chem. Front.*, 2016, **3**, 1559–1565.
43 S. Dhibar, S. Pal, K. Karmakar, S. A. Hafiz, S. Bhattacharjee, A. Roy, S. M. Rahaman, S. J. Ray, S. Dam and B. Saha, *RSC Adv.*, 2023, **13**, 32842–32849.
44 S. Dhibar, S. Pal, S. Some, K. Karmakar, R. Saha, S. Bhattacharjee, A. Roy, S. J. Ray, T. O. Ajiboye, S. Dam and B. Saha, *RSC Adv.*, 2024, **14**, 26354–26361.
45 S. Dhibar, A. Mohan, S. Some, K. Karmakar, S. Babu, S. Bhattacharjee, S. J. Ray, L. N. Nthunya, T. O. Ajiboye, P. Predeep and B. Saha, *Discov Mol.*, 2025, **2**, 11.
46 S. Dhibar, S. Pal, S. Some, K. Karmakar, R. Saha, S. Bhattacharjee, D. Kumari, A. Mohan, T. O. Ajiboye, S. J. Ray, S. Roy, S. Dam and B. Saha, *RSC Adv.*, 2025, **15**, 5214–5219.
47 W.-L. Guan, K. M. Adam, M. Qiu, Y.-M. Zhang, H. Yao, T.-B. Wei and Q. Lin, *Supramol. Chem.*, 2020, **32**, 578–596.
48 E. M. M. Ibrahim, L. H. Abdel-Rahman, A. M. Abu-Dief, A. Elshafaie, S. K. Hamdan and A. M. Ahmed, *Mater. Res. Bull.*, 2018, **107**, 492–497.
49 C. Song, R. Liu, B. Kong, Z. Gu and G. Chen, *Biomed. Technol.*, 2024, **5**, 73–81.
50 Z. Zhang, H. Li, M. Qian, Y. Zheng, L. Bao, W. Cui and D. Wang, *Regen. Biomater.*, 2025, **12**, rbaf004.
51 F. Lin, Y. Li and W. Cui, *Biomed. Technol.*, 2023, **1**, 18–29.
52 E. M. M. Ahmed, L. H. Abdel-Rahman, A. M. Abu-Dief, A. Elshafaie, S. K. Hamdan and A. M. Ahmed, *Phys. Sci.*, 2018, **93**, 055801.
53 S. Khodami, K. Kaniewska, J. Romanski, M. Karbarz and Z. Stojek, *ACS Omega*, 2025, **10**, 12062–12075.
54 S. Sarkar, S. Dutta, S. Chakrabarti, P. Bairi and T. Pal, *ACS Appl. Mater. Interfaces*, 2014, **6**, 6308–6316.
55 S. Anand, R. S. Sundararajan, C. Ramachandraraja, S. Ramalingam and R. Durga, *Spectrochim. Acta, Part A*, 2015, **138**, 203–215.
56 A. Ray and D. N. Sathyanarayana, *Indian J. Chem.*, 1977, **15A**, 306–309.
57 M. Silverstein, G. C. Basseler and C. Morill, *Spectroscopic Identification of Organic Compound*, Wiley, New York, 1981.
58 X. Lin, L. Fu, J. Zhu, W. Yang, D. Li and L. Zhou, *IOP Conf. Ser.: Mater. Sci. Eng.*, 2019, **677**, 032046.
59 M. Zhao, X. Li, Z. Huang, S. Wang and L. Zhang, *Int. J. Biol. Macromol.*, 2021, **172**, 210–222.
60 L. Kergoat, N. Battaglini, L. Miozzo, B. Piro, M.-C. Pham, A. Yassar and G. Horowitz, *Org. Electron.*, 2011, **12**, 1253–1257.
61 T. S. Mahapatra, H. Singh, A. Maity, A. Dey, S. K. Pramanik, E. Suresh and A. Das, *J. Mater. Chem. C*, 2018, **6**, 9756.
62 A. Fernández, A. Redondo, J. Martín-de-León and D. Cantero, *J. Supercrit. Fluids*, 2023, **198**, 105938.
63 X. Fu, G. Zhang, J. Zhang, K. Guo and Y. Pan, *Coatings*, 2018, **8**, 186.
64 S. K. Cheung and N. W. Cheung, Extraction of Schottky diode parameters from forward current-voltage characteristics, *Appl. Phys. Lett.*, 1986, **49**, 85–87.
65 P. N. Murgatroyd, *J. Phys. D Appl. Phys.*, 1970, **3**, 151–156.
66 S. Majumdar, A. Dey, R. Sahu, G. Lepcha, A. Dey, P. P. Ray and B. Dey, *Mater. Res. Bull.*, 2023, **157**, 112003.
67 S. Saha, B. Pal, K. S. Das, P. K. Ghose, A. Ghosh, A. De, A. K. Das, P. P. Ray and R. Mondal, *ChemistrySelect*, 2022, **7**, e202203307.
68 S. Dhibar, A. Dey, S. Majumdar, A. Mandal, P. P. Ray and B. Dey, *New J. Chem.*, 2019, **43**, 15691–15699.
69 H. Wu, J. Zheng, A.-L. Kjøniksen, W. Wang, Y. Zhang and J. Ma, *Adv. Mater.*, 2019, **31**, 1806204.
70 G. Lepcha, S. Majumdar, B. Pal, K. T. Ahmed, I. Pal, B. Satpati, S. R. Biswas, P. P. Ray and B. Dey, *Langmuir*, 2023, **39**, 7469–7483.
71 S. Majumdar, G. Lepcha, K. T. Ahmed, I. Pal, S. R. Biswas and B. Dey, *J. Mol. Liq.*, 2022, **368**, 120619.